12 Surface Physics

T. Greber, J. Kröger, J. Wider, H. J. Neff, C. Cepek, W. Auwärter,
F. Baumberger, M. Hoesch, M. Muntwiler, R. Karrer, W. Deichmann, J. Osterwalder

In the surface physics laboratory we study well-defined surfaces of solid materials as well as adsorbed atomic and molecular monolayers and ultrathin films, prepared under ultrahigh-vacuum (UHV) conditions. In order to measure the geometric arrangement of the atoms within the first few monolayers of the surface we apply predominantly electron-based techniques such as x-ray photoelectron diffraction (XPD), medium-energy electron diffraction (MEED), low-energy electron diffraction (LEED), and more recently also scanning-tunneling and atomic force microscopy (STM/AFM). Angle-resolved UV photoelectron spectroscopy (ARUPS) gives us a detailed picture of the electronic band structure of such systems. Specifically, our experimental setup permits to directly map sections through the Fermi surface, which describes the electronic degrees of freedom relevant for transport properties, magnetic interactions and phase transitions. An important asset of such experiments is that the same probe (photoemission) gives us structural, electronic and magnetic information, and we can therefore study the interplay between these different degrees of freedom on the same sample.

Over the past year we have focused our interest on the following systems: Vicinal Cu(111) surfaces represent lateral nanostructures that can be easily prepared. We have studied the behaviour of the two-dimensional electron gas formed by a surface state in this well-defined and tunable potential energy landscape. For a hydrogen saturated Mo(110) surface, a missing link could be established between observed phonon anomalies and strong Fermi surface nesting. The structural characterization of monolayer hexagonal boron nitride films on Ni(111) has been completed, and the measurement of Fermi surface contours on this system has revealed that the presence of the film strongly modifies the Fermi surface of nickel near the interface. This finding is surprising and very important for the understanding of metal-insulator-metal tunneling junctions. The growth of Co clusters on this *h*-BN film has been characterized by STM, showing a variety of different morphologies that can be controlled by temperature and Co coverage. In a collaboration with Prof. M. Sancrotti (TASC Laboratory of the Istituto Nazionale per la Fisica della Materia, Trieste, Italy) the structural and electronic properties of C_{60} monolayer films on Ag(100) have been investigated. Dr. R. Fasel and Dr. K.-H. Ernst of EMPA Dübendorf have studied the orientation of chiral 7-helicene molecules on various metal surfaces using the XPD capabilities in our surface spectrometer.

Concurrent with these ongoing studies, several new experimental techniques have been pushed forward. In the near-node photoelectron holography project, the first proof-of-principle experiment could be successfully completed during two weeks of beam time at the ALOISA beamline at the Sincrotrone ELETTRA in Trieste. Three near-neighbour shells in a (111) plane of an Al crystal could be imaged at atomic resolution. The development of our picosecond time-resolve MEED experiment has been further delayed due to problems with the sample alignment in the electron scattering chamber. Instead, we have begun to use our femtosecond Ti:sapphire laser system for developing two-photon photoemission (2PPE) spectroscopy in the same angle-mapping mode that we apply for ARUPS. First data measured on Cu(111) clearly show the dispersion of the Shockley surface state (see Section 12.8). These powerful measurement modes will give us unique capabilities for Fermi surface mapping at very low energies that can easily be extended to femtosecond time resolution. Our growing involvement in synchrotron radiation experiments is now fully underway. A new experimental chamber (COPHEE), which is designed to go eventually to the Surface and Interface Spectroscopy beamline of the Swiss Light Source after a temporary deployment to the APE beamline at the Sincrotrone ELETTRA, has produced first test spectra using a laboratory

UV source. A sophisticated extraction electron optical system remains to be designed and built, after which this experiment will permit the spin-resolved measurement of magnetic Fermi surfaces.

We have continued our collaboration with the surface chemistry group of Prof. J. R. Huber of the Physical Chemistry Department (P. Willmott, H. Manoravi, H. Spillmann) who have developed excellent thin film preparation capabilities using pulsed reactive crossed-beam laser ablation. They have grown single crystalline films of technologically relevant GaN and Ti:sapphire, and they were using our photoelectron spectrometer for surface composition analysis and for verifying the crystallinity of their films.

12.1 Surface states on vicinal Cu(111) surfaces

The Shockley (L-gap) surface state on the clean Cu(111) surface provides a low-density two-dimensional free electron gas, which has been used to study quantum interference phenomena in two dimensions [1]. This state is a consequence of the broken translational symmetry in the normal direction at the crystal surface, and it is located in the band gap of the surface-projected bulk bands. The wave functions propagate parallel to the surface and fall off exponentially both towards the vacuum and towards the bulk and are thus quasi two-dimensional. Single monoatomic steps on an otherwise flat surface are known to act as repulsive barriers for surface state electrons [2]. Artificial *periodic* structures of a size appropriate to observe quantum coherence effects are found conveniently on vicinal surfaces: A slight miscut relative to a high symmetry plane of a crystal leads to the formation of terraces bound by a regular step superlattice.

We have studied the Shockley surface state on Cu(332), a surface with a miscut of 10° and a mean (111) terrace length of $\ell = 12$Å. The ARUPS data of Fig. 12.1a show the dispersion of the surface state along $\bar{\Gamma}\bar{M}$ (i.e. perpendicular to the steps). The parabolic dispersion

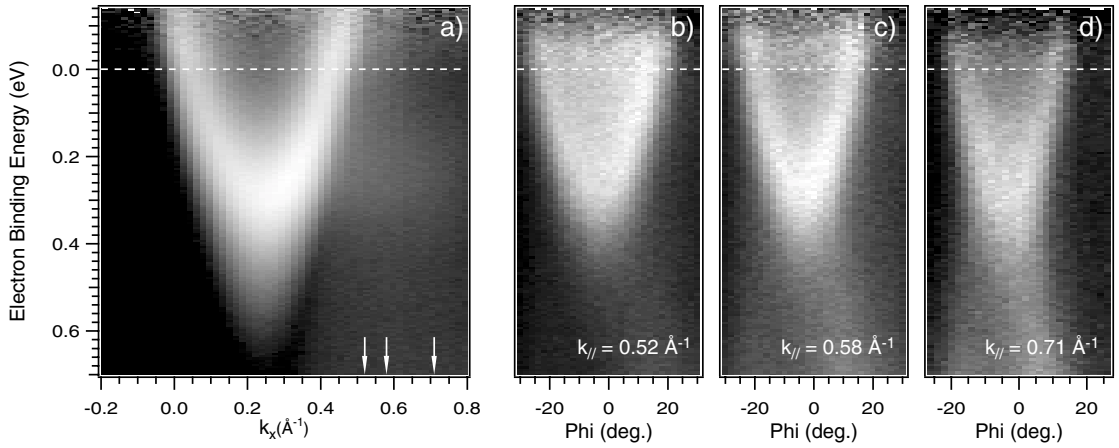

Figure 12.1: *Dispersion plots of the surface state related photoemission feature on Cu(332). a) Polar cut along $\bar{\Gamma}\bar{M}$ (logarithmic gray scale). The arrows indicate the $k_{||}$–values for the measurements shown in (b)-(d), which represent azimuthal cuts in the direction perpendicular to that of (a).*

with an effective mass slightly larger than the value on flat Cu(111) indicates a propagating Bloch state in a periodic potential. The extra intensity on the right hand side of Fig. 12.1a around a binding energy of 0.24 eV is due to a non-dispersing surface state resonance. The

identification of this state as a one–dimensional resonance is confirmed by the azimuthal cuts for $k_{||}$–values larger than $2\pi/\ell$, probing the dispersion of the surface state resonance along the steps (Figs. 12.1b-d). The parabolic dispersion with an effective mass equal to the one on flat Cu(111) indicates free propagation along the steps, while the constant binding energy perpendicular to the steps is a signature of localization in this direction.

12.2 Surface states and surface phonons: H/Mo(110)

In low-dimensional systems the electron-phonon coupling can lead to dramatic effects in the lattice dynamics, inducing strong phonon anomalies. Prominent examples are found on the (110) surfaces of W and Mo. Upon H adsorption, both surfaces show characteristic reductions of phonon frequencies at few and very specific phonon wave vectors. This effect is seen clearly in high-resolution electron energy loss spectra (HREELS) [3] and much more pronounced in helium atom scattering spectra [4]. Recent density functional theory (DFT) calculations [5] support the scenario of a giant Kohn anomaly: The dynamic screening of a specific surface phonon mode of wave vector $\vec{Q}_c$ is dramatically enhanced if the Fermi surface exhibits strong nesting features, i.e. extended parallel sets of contours that can be connected with each other by a single nesting vector $\vec{Q}_c$. Such nesting features provide a large phase space for low-energy excitations that involve the formation of standing electron waves of the same periodicity as the specific surface phonon mode.

While the DFT calculations indicate such nesting features on H/W(110) and H/Mo(110), the experimental situation is less clear. For H/Mo(110) an earlier photoemission study was not able to confirm the nesting properties of the Fermi surface [6].

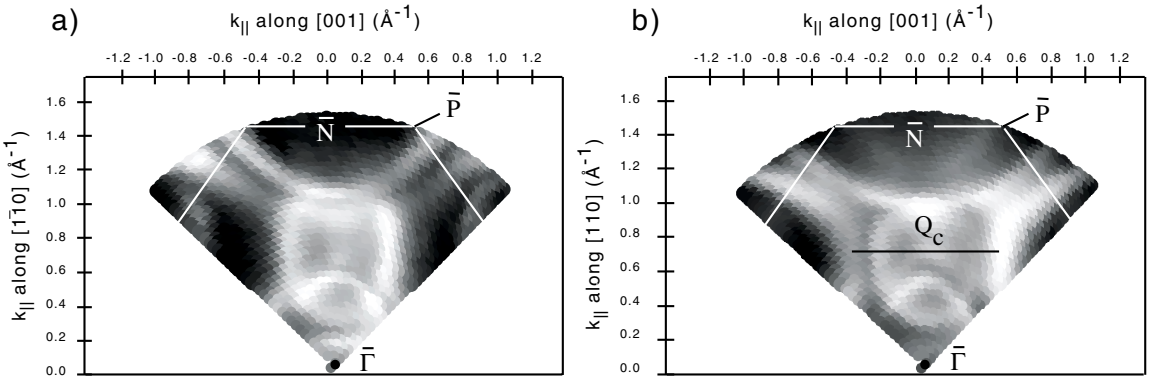

Figure 12.2: *Sector of a high-resolution Fermi surface map of the clean (a) and the hydrogen saturated (b) Mo(110) surface. The photoemission intensity ($h\nu = 21.21eV$) at the Fermi level is plotted in a logarithmic grey scale as a function of $k_{||}$. In both data sets the surface Brillouin zone is indicated as well as high-symmetry points. In b) the nesting vector $\vec{Q}_c$ connecting extended parallel contours is indicated.*

We have repeated this experiment on clean and H-saturated Mo(110), as is summarized in Fig. 12.2. The quarter-pie shaped plots in Figs. 12.2a and b present the high-resolution photoemission measurements of Fermi surface contours within a part of the surface Brillouin zone for the clean Mo(110) surface (a) and for the H-saturated surface (b). The most prominent H-induced change is the splitting off of a contour both on the right and left hand side of a strong bulk-related feature which is not affected itself by H adsorption. These split-off contours form, over a range of the order of 0.4Å^{-1}, straight sections parallel to the $\overline{\Gamma N}$ direction and are thus strongly nested. The corresponding nesting vector measured from these

data amounts to 0.85Å^{-1}. This is in excellent agreement with the nesting vector of 0.86Å^{-1} found in the DFT calculation [5] and is fully consistent with the critical phonon wave vector of 0.90Å^{-1} along the $\overline{\Gamma H}$ direction where the anomaly occurs [3, 4]. We observe similar nesting also perpendicular to the $\overline{\Gamma S}$ direction (not shown) where the comparison of Q_c yields values of 1.19Å^{-1} (photoemission), 1.23Å^{-1} (DFT [5]) and 1.22Å^{-1} [3, 4]. These results provide therefore strong evidence that the mechanism of a giant Kohn anomaly applies for the occurrence of the phonon anomalies on the H-saturated Mo(110) surface.

12.3 Monolayer hexagonal boron nitride film on Ni(111): Thin film geometries from substrate photoelectron diffraction

Metal-insulator-metal structures are very important as tunneling junctions between any combination of normal metals, ferromagnets or superconductors. The ultimate junction is reached with a single monolayer of insulating material. Recently it was discovered that very stable monolayers of hexagonal boron nitride (h-BN) can be prepared by the reaction of benzene-like borazine $(BN)_3H_6$ with Ni(111) at 1100K [7]. With the aim of studying the electronic and magnetic coupling across such films we characterized their growth by XPD and by STM. From the XPD analysis we learned that film growth stops before a second layer starts to form, and the STM images show large and defect-free film terraces [8]. By means of B 1s and N 1s core-level photoelectron diffraction the film structure was determined to be a graphite-like sheet with a slight corrugation of 0.1Å and with the nitrogen atoms terminating the film surface. From this analysis using photoemission from within the film, the registry with the substrate could not be observed, because the electron backscattering off the Ni(111) substrate is extremely weak. However, due to the perfect order in the film, we were able to extract this information from the Ni 2p substrate photoelectron diffraction in the following way [9]:

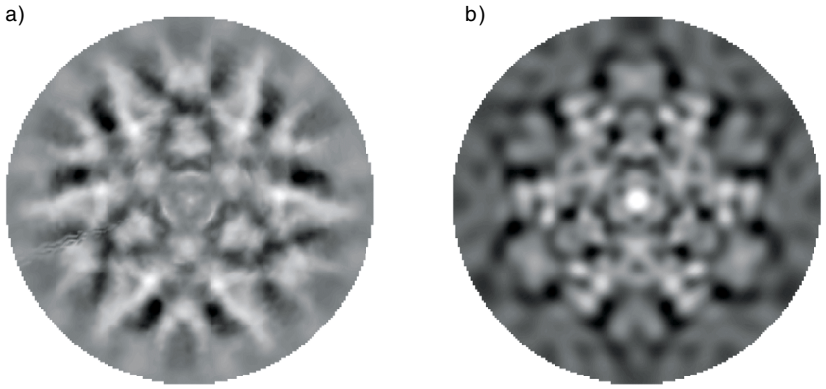

Figure 12.3: *Ni 2p photoelectron diffraction difference plots: In (a), the experimental Ni 2p XPD pattern from the clean Ni(111) surface (E_{kin}=884 eV) is subtracted from the corresponding pattern from the h-BN covered Ni(111) surface after suitable normalization. In (b), the same procedure has been applied to multiple scattering cluster calculations using three Ni(111) substrate layers with and without h-BN film.*

A Ni 2p photoelectron diffraction pattern is measured both for the h-BN covered Ni(111) surface and for the clean surface. The two measurements are suitably normalized and subtracted from each other in order to produce a signature for all scattering processes involving the film. The resulting difference pattern is reproduced in Fig. 12.3a. Unlike regular photoelectron diffraction patterns, where the strong forward focusing effect produces maxima along interatomic vectors, this data set does not give a direct clue to the positions of the atoms in

the film relative to those in the substrate. In substrate emission, atoms from all crystal layers below the surface contribute to the elastic photoemission signal, with an exponential decay away from the surface due to inelastic scattering. At the electron energies used in XPD, typically 10 to 20 atomic layers produce primary photoelectrons that reach the surface and that are coherently scattered by the upper layers and by the film. The difference pattern is therefore a complex superposition of all these coherent and incoherent scattering processes involving the film. By means of multiple scattering cluster calculations the same situation can be modeled by taking the difference of a cluster calculation including the h-BN film and one without. The calculations have been carried out for the three high-symmetry alignments of the film where nitrogen sits either on top or in an fcc or hcp hollow surface site. The best fit to the experimental data was obtained for the N-top site (Fig. 12.3b). Note that the fine structure in the data is modelled quite well, while the choice of grey scale representation makes the general appearance look less similar. However, a quantitative analysis using reliability factors confirms our conclusion, which agrees well with an earlier LEED study by Gamou et al. [10].

12.4 Influence of an atomic grating on a Fermi surface

The electronic structure in metal-insulator interfaces is investigated by means of ARUPS. The single layer h-BN film on Ni(111) described in the preceeding section serves as a model system forming a well defined commensurate (1x1) structure [7, 8, 10]. Fig. 12.4 shows Fermi surface maps of (a) bare Ni(111) and (b) h-BN/Ni(111). They represent the photoemission intensity from the Fermi level as a function of emission angle. In order to probe the same initial states in reciprocal space (k-space) for the two samples, the photon energy was switched from 23.1 eV (He Iβ) for Ni(111) to 21.2 eV (He Iα) for h-BN/Ni(111). This compensates for the work function reduction due to the formation of the h-BN layer.

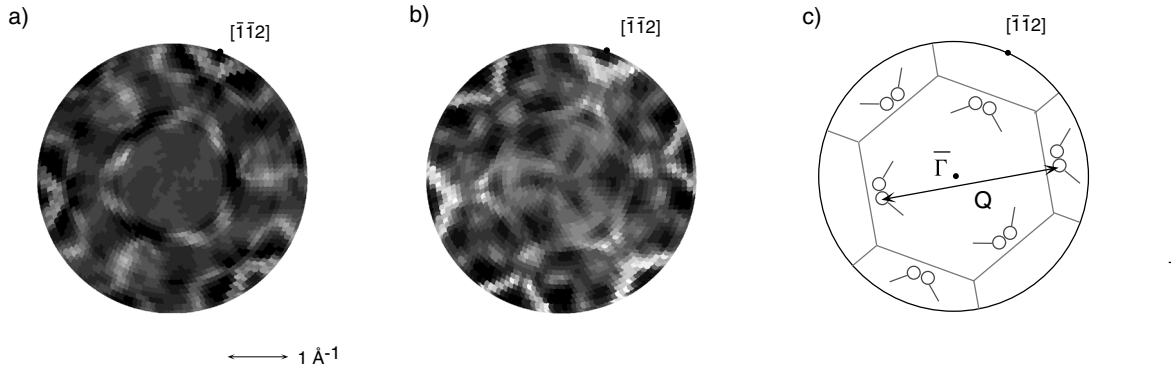

Figure 12.4: *Parallel-projected Fermi surface maps of (a) clean Ni(111) measured with He Iβ radiation and (b) h-BN/Ni(111) measured with He Iα radiation. The high-symmetry direction* [1̄1̄2] *is indicated. c) Schematic drawing of the surface Brillouin zones seen in (a) and (b). The signal disk like features (sp–bands) are replicated in the presence of h-BN by reciprocal surface lattice vectors* $\vec{Q}$.

In comparing Figs. 12.4a and b it can be seen that an insulating overlayer with no electronic states at the Fermi energy nevertheless influences strongly the shape of the Fermi surface in the surface region probed by photoemission. The Fermi surface contours remain three-fold symmetric but get distorted, and new features emerge. In Fig. 12.4c, the surface Brillouin zones covered by these data sets are sketched and particular features are highlighted. The

signal disk like features in Fig. 12.4c correspond to the sp band Fermi surface sheets of nickel which are spin split below the Curie temperature [11]. The most striking influence of the h-BN film is the replication of features of the bare nickel Fermi surface by surface umklapp processes as indicated by the reciprocal surface lattice vector $\vec{Q}$. This clearly reveals that h-BN acts as an atomic grating that modifies the Fermi surface and thus influences physically relevant quantities such as the tunneling characteristics across such junctions.

12.5 Towards well defined metal-insulator-metal junctions

Aiming at a better understanding of electronic and magnetic coupling in metal-insulator-metal (MIM) structures, a system consisting of cobalt clusters on a monolayer h-BN film on Ni(111) is investigated. The insulating h-BN serves as a well defined tunneling barrier [7, 8]. The growth of Co on this flat and defect-free substrate was studied by scanning tunneling microscopy (STM). A wide variety of growth morphologies are found according to the chosen evaporation parameters (see Fig. 12.5). In particular, island size and shape as well as the Co sticking coefficient are strongly temperature dependent. At room temperature (RT) clusters up to 10Å height with only a few nanometers diameter are formed. They tend to arrange themselves in chains, which are aligned along crystallographic high-symmetry directions but not necessarily along steps. The reason for this alignment is not understood at the moment: STM images show no defects in the h-BN film, and magnetic effects are unlikely since reference measurements with Cu clusters (see inset of Fig. 12.5a) show also chain formation. Cobalt evaporation onto a heated substrate leads to triangular-shaped,

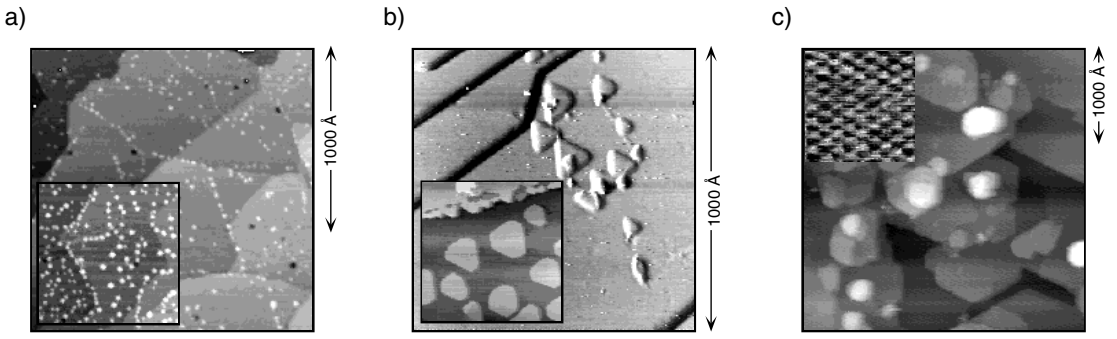

Figure 12.5: *STM images of Co growth on* h-*BN/Ni(111): a) The nanometer-size clusters arranged in chains originate from Co evaporation at room temperature. The inset displays Cu clusters deposited at RT on* h-*BN/Ni(111) showing a similar arrangement. b) Larger two-dimensional triangular-shaped Co islands are produced at* 150°*C. Evaporating Co on bare Ni(111) results in even larger, homogeneously distributed islands of quasi hexagonal shape (inset). c) At higher exposures Co grows three-dimensional. The inset demonstrates atomic resolution on Co.*

two-dimensional islands of several nanometers lateral size (Fig. 12.5b), in contrast to the RT clusters, which are imaged as round objects by the STM. The crystalline structure of these islands is confirmed by recent XPD measurements. Evaporating Co on bare Ni(111) under the same conditions (sample heated to 150 °C) results in even larger, strictly two dimensional islands with quasi hexagonal contours (Fig. 12.5b, inset). Thus, the h-BN layer influences the island growth. Depositing large amounts of Co onto the h-BN film resulted in a rather rough surface: Uncovered h-BN patches coexist with regions of three-dimensional Co islands. Annealing induces a flattening of the surface and a well ordered atomic structure is imaged by STM (Fig. 12.5c).

12.6 Electronic structure of K doped C_{60} monolayers on Ag(100)

In collaboration with M. Sancrotti, TASC-INFM Laboratory, Trieste, Italy

The charge transfer from a Ag(100) surface to a monolayer of adsorbed C_{60} is studied with high-resolution valence band photoelectron spectroscopy. With increasing potassium exposure the progressive filling of the band formed by the lowest unoccupied molecular orbital (LUMO) of C_{60} is observed (Fig. 12.6a). The charge transfer onto the C_{60} molecules is quantified from the observed binding energies of the LUMO derived band (Fig. 12.6b), which can accommodate a total of 6 electrons per C_{60} molecule. In the doping range where the occupancy of the LUMO is $n_{LUMO} < 3$, the LUMO shifts stronger in energy than the highest occupied molecular orbital (HOMO). This non–rigid band shift indicates that the C_{60} molecules get distorted below the LUMO half filling. Furthermore, the intensity of the HOMO is not constant but shows in normal emission a pronounced dip between half and complete LUMO filling (Fig. 12.6c).

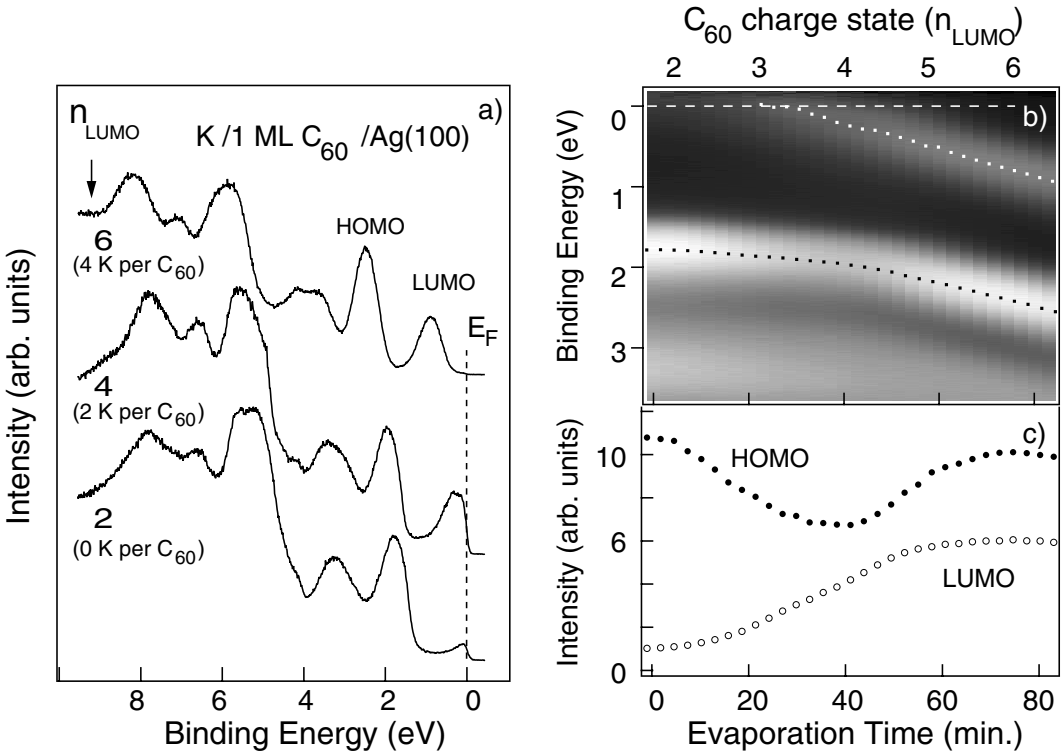

Figure 12.6: *a) Valence band photoemission spectra from a C_{60} monolayer on a Ag(100) surface as a function of LUMO occupancy (n_{LUMO}) and potassium doping; b) Grey scale two–dimensional plot of valence band spectra given as a function of the binding energy and the C_{60} charge state. White and black dots refer to the C_{60} LUMO and HOMO peaks; c) Integrated intensities of the LUMO (white open circles) and HOMO (black dots) emission as a function of the K evaporation time.*

A new method for the quantitative determination of the charge transfer onto C_{60} upon adsorption on a metal surface has been developed. We suppose a linear relationship between the K exposure and the occupancy of the LUMO (n_{LUMO}). Two reference points are determined from the evaporation time where the LUMO is half ($n_{LUMO} = 3$) and completely ($n_{LUMO} = 6$) filled. The LUMO half filling is identified from the crossing of the LUMO peak

maximum with the Fermi level, while the complete filling is found at the point where the photoemission spectrum does not show significant emission from the Fermi level [12]. For the undoped C_{60} monolayer on Ag(001) the method indicates that 1.7 electrons are transferred from the substrate onto C_{60}.

12.7 Near-node photoelectron holography

In collaboration with the ALOISA beamline team at the Sincrotrone ELETTRA, Trieste, Italy

A photoelectron diffraction pattern results from the coherent superposition of a source wave produced by core-level photoemission and a multitude of waves scattered by near neighbour atoms in a single crystal surface. As such, it contains all the prerequisites of a hologram, which is unfortunately perturbed by strong forward scattering effects that dominate over the truly holographic interference features. Near-node photoelectron holography exploits the anisotropic nature of the electron source wave. If the intensity of the photoelectrons is measured close to a node of the source wave, the interference features are enhanced and the holographic reconstruction should lead to a three dimensional image with atomic resolution of the surrounding of the photoemitter [13].

In order to test the idea of near-node photoelectron holography we performed experiments at the ALOISA beamline at the synchrotron facility ELETTRA in Trieste, Italy. We measured Al 2s photoelectron diffraction patterns over a solid angle of nearly 2π in two different experimental geometries (Fig. 12.7c and d). In the near-node geometry (Fig. 12.7a) the angle γ between the polarization of the light $\vec{\varepsilon}$ and the direction of electron detection is 80° whereas in the far-node geometry (Fig. 12.7b) the intensities of the photoelectrons have been measured along the polarization. The holographic reconstruction of the near-node diffraction pattern clearly shows the atomic positions of nearest and next nearest neighbours (Fig. 12.7e). This is not the case in the far-node geometry (Fig. 12.7g). This experimental result indicates that near-node photoelectron holography is a promising way to determine atomic structures at surfaces in a direct way.

12.8 Angle-scanned two-photon photoemission on Cu(111)

Two-photon photoemission (2PPE) is a promising way for exploring occupied and unoccupied electronic states in the vicinity of the Fermi energy at surfaces. It can readily be extended to study excited state lifetimes and dynamics. For such experiments we exploit our femtosecond laser system in combination with the angle-scanned photoemission experiment. Frequency-doubled 400 nm pulses from a Nd:vanadate pumped Ti:sapphire laser with a pulse duration of 80 fs and with 0.6 nJ energy at a repetition rate of 80 MHz are used. The laser light enters a window of the UHV photoemission chamber and is focused on the sample surface. For a surface with a typical work function of 4-5 eV, a single photon ($h\nu = 3.1$eV) is insufficient to excite photoelectrons into the vacuum. In these short pulses, however, the peak power is high enough to produce a considerable amount of two-photon absorption, such that the 2PPE spectrum can be measured.

First 2PPE data taken on clean Cu(111) are shown in Fig. 12.8a, where the spectrum along the surface normal is shown. A Fermi edge is observed at the upper end of the spectrum, as well as a peak near 0.4 eV binding energy that can be identified as the Cu(111) Shockley surface state (see Section 12.1). The peak at the lower end of the spectrum is due to secondary electrons and maybe also due to single-photon photoemission of thermally excited electrons.

In Figure 12.8b, electron energy distribution curves for 60 different emission angles are plotted in a grey scale. Clearly the dispersion of the Shockley surface state is observed. The

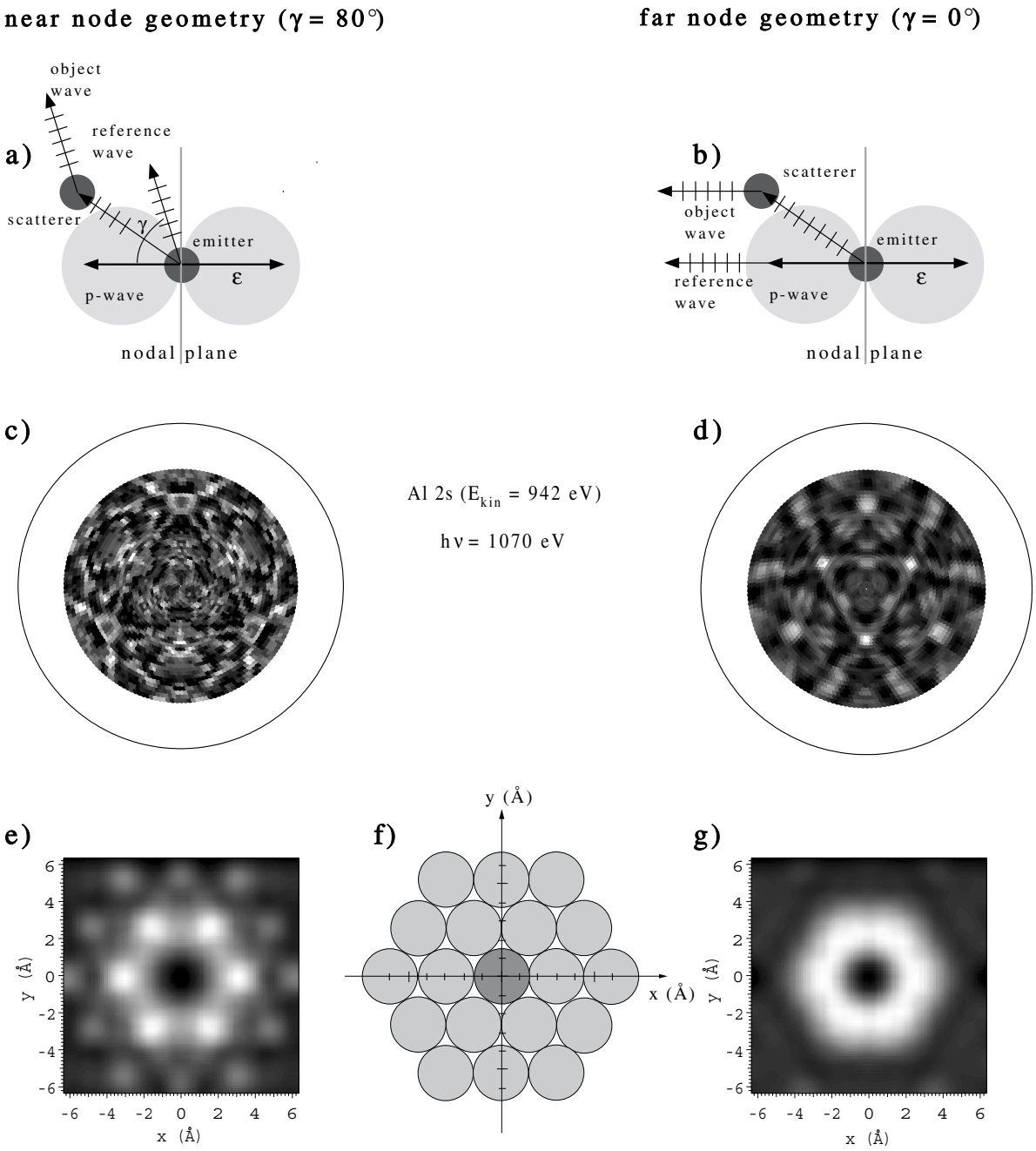

Figure 12.7: *(c) and (d) Experimental Al 2s (E_{kin} = 942 eV) photoelectron diffraction patterns from a clean Al(111) single crystal for two different orientations of the light polarization $\vec{\varepsilon}$ relative to the electron detector. In the near-node geometry (a) the electron intensity is recorded close to the nodal plane of the outgoing p wave whereas in the far-node geometry (b) the electrons are measured perpendicular to the nodal plane. (e) and (g) show corresponding holographic reconstructions within a plane parallel to the surface that contains the emitter. In the near-node image (e) nearest and next nearest neighbours are clearly resolved while in the far-node image (g) the positions of the atoms can not be determined. (f) Hard sphere model of a (111) plane of an Al crystal. The dark disk in the center represents the emitting atom.*

shift of the secondary electron cut-off in going from normal emission to higher polar angles is due to the the inner potential that photoelectrons have to overcome in order to propagate into the vacuum (total internal reflection).

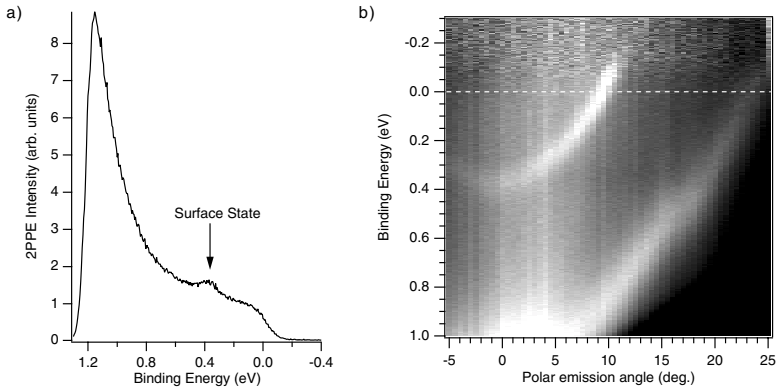

Figure 12.8: *Angle-resolved two-photon photoemission spectra from Cu(111) ($2h\nu = 6.2$ eV, bias voltage = -3.0 V). a) Energy distribution curve at normal emission. The peak at 385 meV binding energy arises from the Shockley surface state. b) Angle-scanned energy distribution curves for 60 different emission angles. The intensities are displayed in a linear gray scale.*

Our electron analyzer has a low transmission for low-energy electrons. Therefore we accelerate the photoelectrons for sensitivity reasons by an electric field that is provided by a negative bias voltage applied to the sample. This field violates parallel momentum conservation for the photoelectrons. The known dispersion of the Shockley surface state (see section 12.1) can be exploited as a reference for the recalibration of the parallel momentum.

12.9 Spin-resolved Fermi surface mapping

In 1999 the setup of a new experimental station running under the ambitious name of *COmplete PHotoEmission Experiment COPHEE)* began, which will be used for spin-resolved photoemission studies with synchrotron radiation. UV photoelectrons are energy analyzed and angle selected by a commercial hemispherical analyzer at high energy resolution and then spin analyzed by Mott scattering. The manipulator used for Fermi surface mapping allows the rotation of the sample to cover the whole hemisphere above its surface. Therefore spin analysis needs to be performed along all three directions of space to reconstruct the full polarization vector. This is achieved by two independent Mott polarimeters. After setup and tests at the Surface Physics Laboratory at the Irchel, the spectrometer will be used at the APE beamline at the Sincrotrone ELETTRA Trieste. Later the whole system will be moved to the Surface and Interface Spectroscopy (SIS) beam-line of the Swiss Light Source at PSI Villigen (under construction).

The home-made variable-temperature sample goniometer (T. Greber) is mounted vertically on the vacuum chamber. A preparation chamber provides standard equipment for sample cleaning, preparation and characterization (LEED) as well as sample transfer to the preparation facilities of the SIS beamline. Below is the μ-metal analysis chamber, which holds a gas-discharge UV-lamp, a twin-anode x-ray tube (Mg K_α and Si K_α) and the photoelectron spectrometer EA125 from Omicron Vakuumphysik GmbH. The electrostatic beam deflection system is currently under development. The two 60 keV Mott detectors were constructed at St. Petersburg Technical University [14]. They employ electrostatic acceleration and focus-

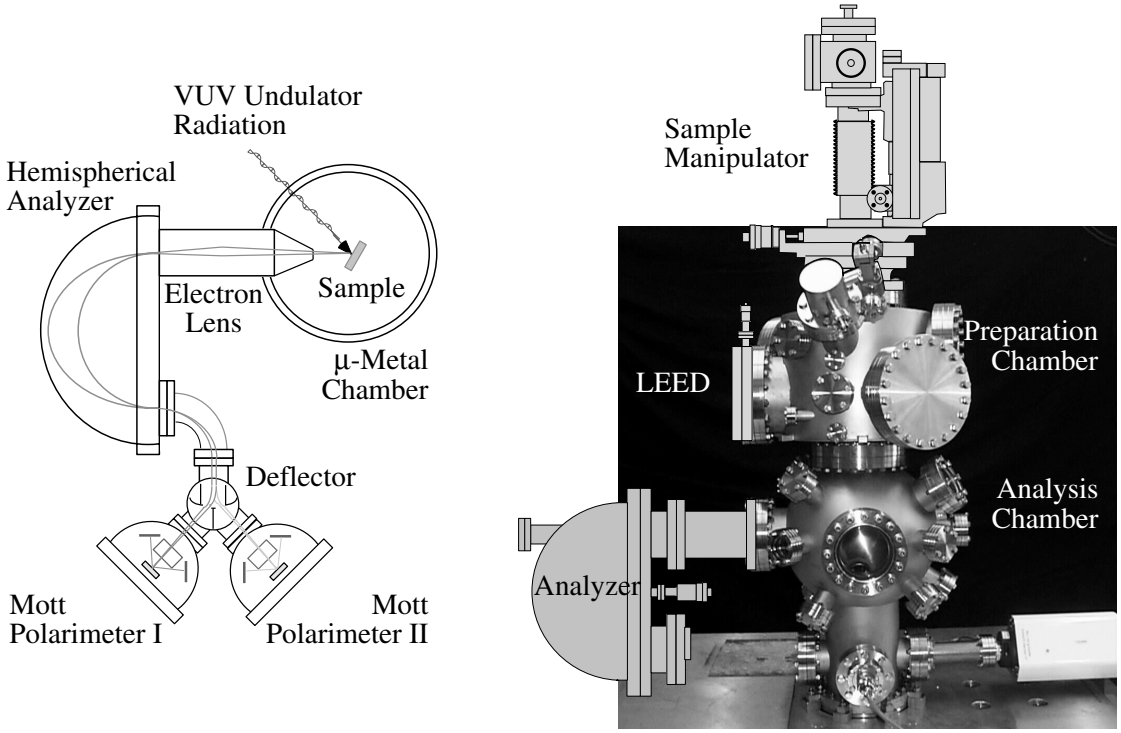

Figure 12.9: Schematic drawing and current status of the setup of COPHEE.

ing, back-scattering off a 80 nm thick gold foil and energy sensitive detection by four silicon surface barrier detectors for each unit.

References

[1] see e.g. M.F. Crommie, C.P. Lutz and D. M. Eigler, Science 262 (1993) 218.

[2] L. Bürgi, O. Jeandupeux, A. Hirstein, H. Brune and K. Kern, Phys. Rev. Lett. 81 (1998) 5370.

[3] J. Kröger, S. Lehwald, H. Ibach, Phys. Rev. B 55, 10895 (1997).

[4] E. Hulpke, J. Lüdecke, Surf. Sci. 287/288 (1993).

[5] B. Kohler, P. Ruggerone, S. Wilke, M. Scheffler, Phys. Rev. Lett. 74, 1387 (1995).

[6] R. H. Gaylord, K. H. Jeong, S. D. Kevan, Phys. Rev. Lett. 62, 2036 (1989).

[7] A. Nagashima, N. Tejima, Y. Gamou, T. Kawai, and C. Oshima, Phys. Rev. B 51, (1995) 4606

[8] W. Auwärter, T.J. Kreutz, T. Greber, J. Osterwalder, Surf. Sci. 429 (1999) 229

[9] M. Muntwiler, Diplomarbeit, Uni Zürich (1999)

[10] Y. Gamou, M. Terai, A. Nagashima, and C. Oshima, Sci. Rep. RITU, A 44 (1997) 211

[11] T.J. Kreutz, T. Greber, P. Aebi, J. Osterwalder, Phys. Rev. B 58 (1998) 1300

[12] M. Merkel, M. Knufer, M. S. Golden, J. Fink, R. Seemann and R. L. Johnson, Phys. Rev. B, 47 (1993) 11470, P. J. Benning, P. Stepniak and J. H. Weaver, Phys. Rev. B, 48 (1993) 9086

[13] T.Greber, J.Osterwalder, Chem. Phys. Lett. 256 (1996) 653 (1996) 653.

[14] V.N. Petrov, M. Landolt, M.S. Galaktionov, B. V. Yushenkov, Rev. Sci. Instr. 68, (1997) 4385